


Multistability of isolated and hydrogenated Ga–O divacancies in  $\beta$ -Ga<sub>2</sub>O<sub>3</sub>

Y. K. Frodason,<sup>1,\*</sup> C. Zimmermann,<sup>1</sup> E. F. Verhoeven,<sup>1</sup> P. M. Weiser,<sup>1</sup> L. Vines,<sup>1</sup> and J. B. Varley<sup>2</sup>  
<sup>1</sup>Department of Physics/Centre for Materials Science and Nanotechnology, University of Oslo, N-0318 Oslo, Norway  
<sup>2</sup>Lawrence Livermore National Laboratory, Livermore, California 94550, USA

 (Received 3 December 2020; accepted 12 January 2021; published 3 February 2021)

This work systematically explores 19 unique configurations of the close-associate Ga–O divacancies ( $V_{\text{Ga}}V_{\text{O}}$ ) in  $\beta$ -Ga<sub>2</sub>O<sub>3</sub>, including their complexes with H impurities, using hybrid functional calculations. Interestingly, most configurations are found to retain the negative- $U$  behavior of  $V_{\text{O}}$ , as they exhibit a thermodynamic ( $-/3-$ ) charge-state transition level energetically located in the upper part of the band gap, where the  $3-$  charge state is associated with the formation of a Ga–Ga dimer. The energy positions of the thermodynamic ( $-/3-$ ) charge-state transition levels divide the divacancy configurations into three different groups, which can be understood from the three possible Ga–Ga dimerizations resulting from the tetrahedral and octahedral Ga sites. The relative formation energies of the different divacancy configurations, and hence the electrical activity of the divacancies, is found to depend on the Fermi-level position, and the energy barriers for transformation between different divacancy configurations are explored from nudged elastic band calculations. Hydrogenation of the divacancies is found to either passivate their negative- $U$  charge-state transition levels or shift them down in Fermi level position, depending on whether the H resides at  $V_{\text{O}}$  or forms an O–H bond at  $V_{\text{Ga}}$ , respectively. Finally, the divacancy is discussed as a potential origin of the so-called  $E_2^*$  center previously observed by deep-level transient spectroscopy.

DOI: [10.1103/PhysRevMaterials.5.025402](https://doi.org/10.1103/PhysRevMaterials.5.025402)

## I. INTRODUCTION

Monoclinic gallium sesquioxide ( $\beta$ -Ga<sub>2</sub>O<sub>3</sub>) has recently attracted substantial research interest. The combination of an ultra-wide band gap ( $\sim 4.9$  eV), high and controllable  $n$ -type conductivity, and availability of large-area single-crystal substrates, renders  $\beta$ -Ga<sub>2</sub>O<sub>3</sub> an attractive material for high-power electronics and applications requiring UV transparency [1]. However, the advancement of  $\beta$ -Ga<sub>2</sub>O<sub>3</sub>-based devices will require knowledge about the properties and origin of prominent deep-level defects, as they can potentially have a severe impact on the performance and stability of devices [2]. For example, McGlone *et al.* [3,4] reported that the  $E_2^*$  center, observed by deep-level transient spectroscopy (DLTS), is limiting the performance of  $\beta$ -Ga<sub>2</sub>O<sub>3</sub>-based field-effect transistors.

$E_2^*$  is an electron trap with an activation energy of about 0.75 eV [5] (not to be confused with  $E_2$  [6,7]), and has been observed in  $\beta$ -Ga<sub>2</sub>O<sub>3</sub> layers grown by plasma-assisted molecular beam epitaxy [3,4].  $E_2^*$  can be generated by proton irradiation with a close to linear dose dependence after subsequent heat treatments at around 650 K, suggesting a relation to an intrinsic-related defect complex that is formed by a thermally activated process [5,6]. Recently, the authors of this article reported on the formation of  $E_2^*$  in  $\beta$ -Ga<sub>2</sub>O<sub>3</sub> subjected to H and/or He implantation, as measured by DLTS on Schottky barrier diodes. It was found that the introduction of  $E_2^*$  is promoted when performing a subsequent annealing

at 650 K under an applied reverse-bias voltage (reverse-bias annealing) [8]. Conversely, heat treatments without an applied reverse-bias voltage (zero-bias annealing) lead to a decrease in the  $E_2^*$  concentration, which is more pronounced in the presence of H. Moreover, simulations of DLTS spectra suggest that  $E_2^*$  consists of several overlapping signatures [8]. Based on these experimental results, it was proposed that the most likely origin of  $E_2^*$  is a defect complex involving intrinsic defects, which can interact with H donors, and exist in several different configurations, where the configurations giving rise to  $E_2^*$  are more likely to form when the Fermi level is shifted away from the conduction band minimum (CBM), i.e., in the space-charge region of Schottky barrier diodes. Based on previously reported theoretical calculations on intrinsic defects in  $\beta$ -Ga<sub>2</sub>O<sub>3</sub> [5], divacancy complexes were put forward as a potential defect origin for  $E_2^*$  [8]. One of the focal points of the present study is to investigate this proposed defect model.

Gallium and oxygen vacancies ( $V_{\text{Ga}}$  and  $V_{\text{O}}$ , respectively) have drawn considerable attention as native defects that are likely to be present in both as-grown and processed  $\beta$ -Ga<sub>2</sub>O<sub>3</sub> [9]. Indeed, first-principles calculations support that a sizable equilibrium concentration of  $V_{\text{Ga}}$  is expected under  $n$ -type conditions, while the concentration of  $V_{\text{O}}$  is expected to be higher in compensated material [10–14]. Moreover, hybrid functional calculations show that  $V_{\text{Ga}}$  is an exceedingly deep triple acceptor that can bind up to four holes in polaronic states, resulting in charge states ranging from  $1+$  to  $3-$  in the band gap [15].  $V_{\text{O}}$  acts as a deep double donor exhibiting negative- $U$  behavior [15]. However, none of the monovacancies exhibit any thermodynamic charge-state transition levels with Fermi-level positions compatible with the measured

\*ymirkf@fys.uio.no

activation energy of about 0.75 eV for the  $E_2^*$  level [8], as they are located in excess of 1.6 eV below the CBM [5].

Considering the acceptor and donor nature of  $V_{\text{Ga}}$  and  $V_{\text{O}}$ , respectively, as well as the high mobility predicted for  $V_{\text{Ga}}$  relative to  $V_{\text{O}}$  [13], it is conceivable that  $V_{\text{Ga}}$  can migrate and complex with available  $V_{\text{O}}$ , forming stable close-associate Ga–O divacancies ( $V_{\text{Ga}}V_{\text{O}}$ ). Divacancies are also likely to be introduced by H- or He implantation. For example, Holston *et al.* [16] observed an EPR signal in neutron-irradiated ZnO, which they assigned to the Zn–O divacancy. Moreover, both isolated and hydrogenated divacancies have been identified in H-implanted silicon [17]. However, seeing as there are three off-site configurations of  $V_{\text{Ga}}$  in  $\beta\text{-Ga}_2\text{O}_3$  [5], in addition to the five simple monovacancies, the resulting  $V_{\text{Ga}}V_{\text{O}}$  can occur in a plethora of different configurations. This large configuration space can make experimental identification challenging. In such cases, first-principles defect calculations can be particularly useful, as all configurations can be explored and compared. In this work, we have performed hybrid functional calculations to shed light on the relative stability of the 19 crystallographically inequivalent close-associate  $V_{\text{Ga}}V_{\text{O}}$  configurations, and the energy barriers for transformation between different configurations, revealing trends in their electrical properties that can be useful to categorize them. We also investigate defect complexes between divacancies and H. Finally, we discuss the isolated and hydrogenated divacancy as a potential candidate for the aforementioned  $E_2^*$  center [8].

## II. METHODOLOGY

First-principles calculations were based on the generalized Kohn-Sham theory with the projector augmented wave (PAW) method [18,19], as implemented in VASP [20]. The Ga  $3d$  electrons were treated as valence electrons, unless specified otherwise. To obtain an accurate description of the electronic and structural properties of  $\beta\text{-Ga}_2\text{O}_3$ , we used the Heyd-Scuseria-Ernzerhof (HSE) [21] range-separated hybrid functional, with the fraction of screened Hartree-Fock exchange set to  $\alpha = 0.33$  [22]. This results in a direct band gap of 4.9 eV, and lattice parameters  $a = 12.23$  Å,  $b = 3.03$  Å, and  $c = 5.79$  Å, in good agreement with experimental data [23,24].

For defect calculations, we employed 160-atom supercells, a plane-wave energy cutoff of 400 eV, and a single special  $k$  point at (0.25, 0.25, 0.25). Defect formation energies and thermodynamic charge-state transition levels were calculated by following the established formalism [25], e.g., the formation energy of  $(V_{\text{Ga}}V_{\text{O}})^q$  is given by

$$E_f^q = E_{\text{tot}}^q(V_{\text{Ga}}V_{\text{O}}) - E_{\text{tot}}(\text{bulk}) + \mu_{\text{Ga}} + \mu_{\text{O}} + q\epsilon_F, \quad (1)$$

where  $q$  is the charge state of the defect,  $E_{\text{tot}}^q(V_{\text{Ga}}V_{\text{O}})$  and  $E_{\text{tot}}(\text{bulk})$  are the total energies of the  $(V_{\text{Ga}}V_{\text{O}})^q$  containing and pristine supercells, respectively,  $\mu_{\text{Ga}}$  and  $\mu_{\text{O}}$  are chemical potentials for the removed Ga and O atoms, and  $\epsilon_F$  is the Fermi-level position, relative to the valence band maximum (VBM). The chemical potential values can vary between Ga- and O-rich limits. These limits correspond to upper bounds on  $\mu_{\text{Ga}}$  and  $\mu_{\text{O}}$ , respectively, which are given by the total energy per atom of Ga and  $\text{O}_2$ . The Ga- and O-rich limits impose lower bounds on the corresponding other species through the

thermodynamic stability condition, given by

$$2\Delta\mu_{\text{Ga}} + 3\Delta\mu_{\text{O}} = \Delta H_f(\beta\text{-Ga}_2\text{O}_3), \quad (2)$$

where  $H_f(\beta\text{-Ga}_2\text{O}_3)$  is the enthalpy of formation of  $\beta\text{-Ga}_2\text{O}_3$ .  $\mu_{\text{H}}$  is referenced to the total energy per atom of  $\text{H}_2$ , with  $\text{H}_2\text{O}$  as a limiting phase under O-rich conditions [26]. All formation energies presented here are for the O-rich limit, but the Ga-rich formation energy can be obtained by adding 1.71 eV and then subtracting 1.35 eV for every H atom in the divacancy complex. For charged defects, the total energies were corrected by using the anisotropic [27] Freysoldt, Neugebauer, and Van de Walle (FNV) scheme [28], using the static dielectric tensor [29].

Divacancy transformation energy barriers were calculated using the climbing image nudged elastic band method (CI-NEB) [30] with five images, and converging the forces to within 50 meV/Å. Due to high computational cost, the CI-NEB calculations were performed using a PAW potential that included the Ga  $3d$  electrons in the core, but keeping the lattice parameters fixed to those computed by treating the  $3d$  electrons explicitly.

## III. RESULTS AND DISCUSSION

We first establish the notation for the different  $V_{\text{Ga}}V_{\text{O}}$  configurations that were investigated. The monoclinic  $\beta\text{-Ga}_2\text{O}_3$  structure has two inequivalent Ga sites (Ga1 and Ga2), and three inequivalent O sites (O1, O2, and O3). The coordination number is four for the Ga1 site ( $1 \times \text{O1}$ ,  $2 \times \text{O2}$ ,  $1 \times \text{O2}$ ), six for the Ga2 site ( $2 \times \text{O1}$ ,  $1 \times \text{O2}$ ,  $3 \times \text{O2}$ ), three for the O1 ( $2 \times \text{Ga2}$ ,  $1 \times \text{Ga1}$ ) and O2 sites ( $2 \times \text{Ga1}$ ,  $1 \times \text{Ga2}$ ), and four for the O3 site ( $3 \times \text{Ga2}$ ,  $1 \times \text{Ga1}$ ).

The regular monovacancies are denoted by  $V_{\text{Ga1}}$ ,  $V_{\text{Ga2}}$ ,  $V_{\text{O1}}$ ,  $V_{\text{O2}}$  and  $V_{\text{O3}}$ . The three additional off-site configurations of  $V_{\text{Ga}}$  are denoted by  $V_{\text{Ga}}^{\text{ia}}$ ,  $V_{\text{Ga}}^{\text{ib}}$  and  $V_{\text{Ga}}^{\text{ic}}$  [5]. Figure 1 shows all five  $V_{\text{Ga}}$  configurations, with the nearest-neighbor O sites being labeled. Depending on which O atom is removed, 19 inequivalent  $V_{\text{Ga}}V_{\text{O}}$  configurations can occur (only close-associate vacancy pairs are considered). The divacancies are named according to the labels in Fig. 1, e.g., if the O2 atom next to  $V_{\text{Ga2}}$  is removed, the resulting divacancy is denoted by  $V_{\text{Ga2}}V_{\text{O2}}$ .

### A. Isolated divacancies

#### 1. Formation energies and electronic properties

Figure 2(a) shows the formation energy of  $V_{\text{Ga}}V_{\text{O}}$  under O-rich conditions. We note that choosing different chemical conditions does not change the relative energetics of the divacancies or their reported transition levels. The divacancy configurations exhibiting formation energies of more than 1 eV above the lowest energy configuration for all relevant Fermi level positions (i.e., the upper half of the band gap, considering  $\beta\text{-Ga}_2\text{O}_3$  as primarily being  $n$ -type or semi-insulating [31]) have been omitted for the sake of readability, but the formation energies of all configurations can be found in Ref. [32]. Moreover, the  $V_{\text{Ga}}^{\text{ia}}V_{\text{O1a}}$  and  $V_{\text{Ga}}^{\text{ia}}V_{\text{O1b}}$  configurations were found to spontaneously revert back to  $V_{\text{Ga2}}V_{\text{O1}}$  and  $V_{\text{Ga1}}V_{\text{O1}}$  upon ionic relaxation, respectively, and are thus omitted from further discussion.

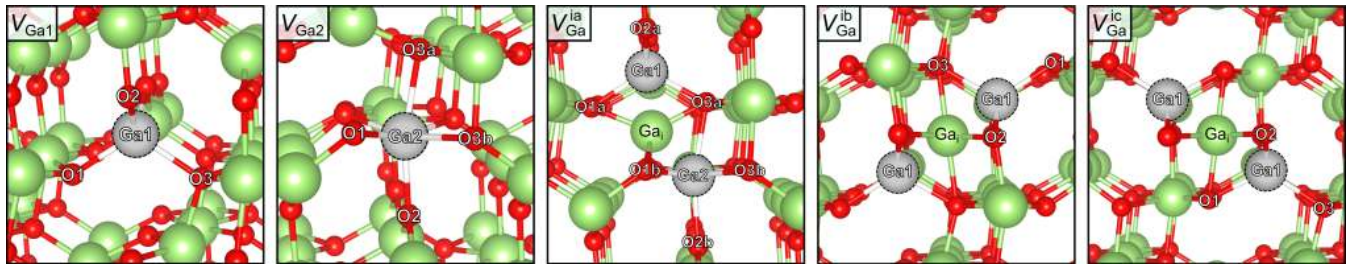


FIG. 1. Ball-and-stick structures indicating the crystallographically inequivalent nearest-neighbor O atoms for each  $V_{Ga}$  configuration. The Ga and O atoms are green and red, respectively, and the vacancies are indicated by translucent circles with dashed outlines. In total, 19 unique close-associate  $V_{Ga}V_O$  configurations can be found depending on which O atom is removed.

Seeing as  $V_{Ga}V_O$  combines a double donor with a triple acceptor, one might expect the divacancy to act overall as a single acceptor. However, for the majority of divacancy configurations, we find that two electrons can be captured in a deep defect state at  $V_O$ , resulting in a triple acceptor. As shown in Fig. 2(b), the two electrons in this deep defect state are mainly shared between two Ga ions associated with the

$V_O$ , which undergo a large lattice relaxation to form a Ga–Ga dimer. Notably, the thermodynamic charge-state transition goes directly from 1– to 3–, which means that the negative- $U$  behavior of the isolated  $V_O$  is retained [10] (the effective correlation energy  $U$  for three successive charge states  $q_1$ ,  $q_2$  and  $q_3$  of a defect  $d$  is given by  $U = E_f^{q_1}(d) + E_f^{q_3}(d) - 2E_f^{q_2}(d)$  [33,34]). Furthermore, we find that all  $V_{Ga}V_O$  configurations can bind up to three holes in polaronic states at  $V_{Ga}$ , resulting in charge states ranging from 2+ to 1– or 3– within the band gap, depending on the divacancy configuration. This makes  $V_{Ga}V_O$  a highly electrically active defect, with a behavior similar to that previously reported for the Zn–O divacancy in ZnO [35], where  $V_O$  also exhibits a deep (2+ / 0) level [36–38].

Interestingly, the thermodynamic (–/3–) transition levels fall within two narrow Fermi level ranges, as highlighted by the grey vertical bars in Fig. 2(a). Upon closer inspection, the common feature of the configurations in each range is that they share the same type of Ga–Ga dimer. Those with levels at around 1.4 and 0.5 eV below the CBM exhibit Ga1–Ga1 and Ga1–Ga2 dimers, respectively, and the divacancy configurations that could not be stabilized in the 3– charge state exhibit Ga2–Ga2 dimers. It should be noted that the (–/3–) transition levels for some of the configurations with a Ga2–Ga2 dimer occur just barely outside the band gap, e.g., 0.03 eV above the CBM for  $V_{Ga1}V_{O1}$ . Furthermore, for certain high-energy divacancy configurations involving  $V_{O3}$ , additional Ga ions are involved in the deep defect state, resulting in slight deviations in the positions of their (–/3–) transition levels compared to the Fermi-level ranges highlighted in Fig. 2(a). In any case, the defect states involving Ga1 ions tend to be significantly deeper than those involving Ga2 ions, which is likely due to the lower coordination number of the Ga1 site compared to Ga2. This trend is also found for the isolated  $V_O$ , where the deepest  $V_{O2}$  has two adjacent Ga1 ions, while  $V_{O1}$  and  $V_{O3}$  have only one adjacent Ga1 ion.

The relative formation energy of the different divacancy configurations depends on the position of the Fermi level, as shown in Fig. 2(a). Focusing on the upper part of the band gap,  $V_{Ga2}V_{O2}$  or  $V_{Ga}^{ib}V_{O1}$  are lowest in formation energy when the Fermi level is above or below 4.53 eV, respectively. For the  $V_{Ga2}V_{O2}$  configuration, however, the closely related  $V_{Ga}^{ia}V_{O2}^a$  (see Fig. 1) is only slightly higher in formation energy. This is similar to the isolated  $V_{Ga}$  case, where the  $V_{Ga2}$  and  $V_{Ga}^{ia}$  configurations are also close in formation energy [6]. Considering the typical unintentional  $n$ -type conductivity of

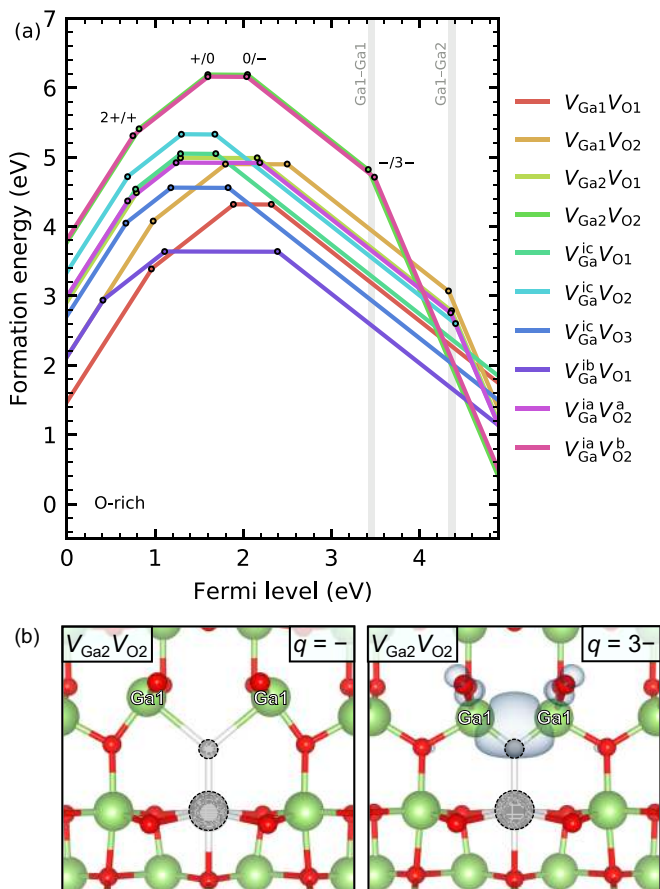


FIG. 2. (a) Formation energy of the most favorable  $V_{Ga}V_O$  configurations under O-rich conditions. The grey bars highlight the Fermi level region with (–/3–) transitions for divacancies with Ga1–Ga1 or Ga1–Ga2 dimerization. (b) Relaxed structures of  $V_{Ga2}V_{O2}$ , showing the deep defect state (blue isosurface) associated with the large lattice distortion to form a Ga1–Ga1 dimer when going from  $q = -$  to  $q = 3-$ .

$\beta$ -Ga<sub>2</sub>O<sub>3</sub> [31], the calculated formation energy of  $V_{\text{Ga}}V_{\text{O}}$  is relatively low, i.e., when the Fermi level is at the CBM, the formation energy of  $V_{\text{Ga}2}V_{\text{O}2}$  is 0.48 and 2.18 eV in the O- and Ga-rich limits, respectively. This is sufficiently low for divacancies to be incorporated in appreciable concentrations during materials growth or processing.

To investigate the thermal stability of the divacancy, binding energies were calculated as the difference in formation energy between the divacancy and the sum of the formation energies of its monovacancy constituents, e.g., for  $V_{\text{Ga}2}V_{\text{O}2}$  the binding energy is calculated as

$$E_{\text{b}} = [E_{\text{f}}(V_{\text{Ga}2}) + E_{\text{f}}(V_{\text{O}2})] - E_{\text{f}}(V_{\text{Ga}2}V_{\text{O}2}), \quad (3)$$

which means that a positive binding energy will result in a stable complex. We note that the chemical conditions do not change the calculated binding energies. However, the calculated binding energy depends on the Fermi level position, as both the divacancy and its constituents exhibit charge-state transition levels within the band gap. A binding energy diagram with all divacancy configurations is included in Ref. [32]. The  $V_{\text{Ga}2}V_{\text{O}2}$  configuration exhibits a binding energy of 1.60 eV under *n*-type conditions, and up to 3.01 eV when the Fermi-level position is around mid-gap. Once formed, the  $V_{\text{Ga}}V_{\text{O}}$  complex is thus predicted to show a high thermal stability. These high binding energies can be rationalized by considering the fact that Ga–O vacancy pairing lowers the number of dangling bonds. Moreover, for the singly negatively charged divacancies, there will be a strong Coulomb attraction between  $V_{\text{Ga}}^{3-}$  and  $V_{\text{O}}^{2+}$ .

To summarize, the low formation energies of the vacancies combined with a relatively low migration energy of  $V_{\text{Ga}}$  [13], and the high stability of the divacancies, suggests that divacancies are important defect complexes likely to be found in processed material and devices.

## 2. Interplay between divacancy configurations

The relative stability of the different divacancy configurations depends on the Fermi-level position, which means that a change in Fermi-level position can induce a change in divacancy configuration. However, the transformation from a local-minimum to a global-minimum divacancy configuration is not necessarily an instantaneous process, as there might exist large energy barriers to switch between different divacancy configurations. To investigate the interplay between different divacancy configurations at elevated temperatures, CI-NEB calculations were performed to find the minimum energy path between different configurations separated by a single Ga or O jump (e.g.,  $V_{\text{Ga}2}V_{\text{O}2}$  and  $V_{\text{Ga}2}V_{\text{O}1}$ ). The transformation energy barrier  $E_{\text{t}}$  is determined as the total energy difference between the initial configuration and the saddle point configuration. The temperature at which a transformation with a given  $E_{\text{t}}$  becomes possible is estimated based on a thermally activated process with a jump rate given by [39]

$$\Gamma = \Gamma_0 \exp(-E_{\text{t}}/k_{\text{B}}T_{\text{a}}), \quad (4)$$

where  $\Gamma_0$  is the attempt frequency. If  $\Gamma_0$  is assumed to be a typical phonon frequency of 10 THz, and the jump rate at which reorientation becomes observable is set to 1 min<sup>-1</sup>, the annealing temperature can be obtained as

$T_{\text{a}}/E_{\text{m}} \approx 341$  K/eV [39]. We again focus on the Fermi-level positions in the upper half of the band gap, which means that we only consider singly and triply negatively charged divacancies. Due to the high-computational cost of hybrid functional CI-NEB calculations, we also limit the analysis to the divacancy configurations with the lowest formation energy, i.e., those shown in Fig. 2(a). Table I lists the resulting transformation energy barriers, where the top five rows involve O jumps, and the remaining rows involve Ga jumps. The saddle point structures for the transformations in Table I are shown in Ref. [32].

Previously reported CI-NEB calculations on monovacancies in  $\beta$ -Ga<sub>2</sub>O<sub>3</sub> by Kyrtsov *et al.* [13] have shown significantly higher migration barriers for  $V_{\text{O}}^0$  compared to  $V_{\text{O}}^{2+}$ . The same trend is evident from the divacancy transformations involving O jumps, as the calculated transformation energy barriers are significantly higher for  $(V_{\text{Ga}}V_{\text{O}})^{3-}$  compared to  $(V_{\text{Ga}}V_{\text{O}})^-$ . For Ga jumps, the opposite trend is found for cases where the jumping Ga ion is immediately adjacent to  $V_{\text{O}}$  in the divacancy, e.g.,  $V_{\text{Ga}2}V_{\text{O}2} \rightleftharpoons V_{\text{Ga}1}V_{\text{O}2}$ .

However, transformations to or from off-site  $V_{\text{Ga}}$  configurations, e.g.,  $V_{\text{Ga}1}V_{\text{O}1} \rightleftharpoons V_{\text{Ga}}^{\text{ib}}V_{\text{O}1}$ , are relatively insensitive to the charge state. Furthermore, we find that Ga jumps generally exhibit significantly lower transformation barriers compared to O jumps, which is also consistent with results reported by Kyrtsov *et al.* [13].

The large calculated migration barriers for divacancy transformations involving O jumps in the 3- charge state means that high temperatures are necessary to reach all configurations under *n*-type conditions. For example,  $T_{\text{a}}$  in excess of 1200 K is required to transform from  $V_{\text{Ga}2}V_{\text{O}2}$  to  $V_{\text{Ga}2}V_{\text{O}1}$ , based on the 3.62 eV barrier in the 3- charge state. Thus, depending on the temperature, only a subset of the configurations can be accessed, which could potentially prevent local-minimum divacancy configurations from finding the global-minimum configuration.

## B. Hydrogenated divacancies

Hydrogen is a ubiquitous impurity, and can form complexes with defects in  $\beta$ -Ga<sub>2</sub>O<sub>3</sub>, including  $V_{\text{Ga}}$  [40,41] and  $V_{\text{O}}$  [10]. Hydrogen interstitials ( $\text{H}_{\text{i}}$ ) are predicted to act as shallow donors, and are highly mobile, making them likely to be trapped by  $V_{\text{Ga}}V_{\text{O}}$  acceptors [10]. In the resulting defect complex, H can either occupy  $V_{\text{O}}$ , or form an O–H bond at  $V_{\text{Ga}}$ , which is denoted by  $\text{H}_{\text{O}}$  and  $V_{\text{Ga}}\text{H}$ , respectively. The corresponding hydrogenated divacancies are here denoted by  $V_{\text{Ga}}\text{H}_{\text{O}}$  and  $V_{\text{Ga}}\text{H}-V_{\text{O}}$ .

### Formation energies and electronic properties

Figures 3(a) and 3(b) show the formation energies of hydrogenated divacancies with one or two trapped H atoms, respectively, under O-rich conditions. Again, only the configurations exhibiting formation energies within 1 eV of the lowest energy configuration under the relevant Fermi-level positions are shown. Other explored configurations can be found in Ref. [32]. H trapping at the divacancy introduces a shallow donor state for both the  $V_{\text{Ga}}\text{H}-V_{\text{O}}$  and  $V_{\text{Ga}}\text{H}_{\text{O}}$  configurations, thus passivating a single  $V_{\text{Ga}}$  acceptor state. However, for the latter configuration, the conversion of  $V_{\text{O}}$  into a shallow  $\text{H}_{\text{O}}$

TABLE I. Migration barriers for transformation between divacancy configurations in the 3− and 1− charge states, given in units of eV. The arrows indicate the direction of the transformation, according to the divacancy transformation in the left column. The top five rows of the table involve O jumps, while the remaining rows involve Ga jumps. For these calculations, Ga 3*d* electrons were included in the core.

Divacancy transformation	$E_t$ (eV)			
	$q = 1-$		$q = 3-$	
	$\rightarrow$	$\leftarrow$	$\rightarrow$	$\leftarrow$
$V_{\text{Ga}1}V_{\text{O}1} \rightleftharpoons V_{\text{Ga}1}V_{\text{O}2}$	2.21	1.31	3.31	3.81
$V_{\text{Ga}2}V_{\text{O}2} \rightleftharpoons V_{\text{Ga}2}V_{\text{O}1}$	0.99	2.19	3.62	2.83
$V_{\text{Ga}}^{\text{ic}}V_{\text{O}1} \rightleftharpoons V_{\text{Ga}}^{\text{ic}}V_{\text{O}2}$	1.57	1.26	2.70	3.45
$V_{\text{Ga}}^{\text{ic}}V_{\text{O}1} \rightleftharpoons V_{\text{Ga}}^{\text{ic}}V_{\text{O}3}$	4.01	4.39	4.82	4.85
$V_{\text{Ga}}^{\text{ic}}V_{\text{O}2} \rightleftharpoons V_{\text{Ga}}^{\text{ic}}V_{\text{O}3}$	1.75	2.43	4.50	3.78
$V_{\text{Ga}1}V_{\text{O}1} \rightleftharpoons V_{\text{Ga}2}V_{\text{O}1}$	2.81	2.20	0.69	none
$V_{\text{Ga}1}V_{\text{O}1} \rightleftharpoons V_{\text{Ga}}^{\text{ib}}V_{\text{O}1}$	0.55	1.10	0.56	1.14
$V_{\text{Ga}1}V_{\text{O}1} \rightleftharpoons V_{\text{Ga}}^{\text{ic}}V_{\text{O}1}$	0.69	0.81	0.64	1.00
$V_{\text{Ga}1}V_{\text{O}2} \rightleftharpoons V_{\text{Ga}}^{\text{ic}}V_{\text{O}2}$	0.37	1.03	0.37	0.95
$V_{\text{Ga}2}V_{\text{O}2} \rightleftharpoons V_{\text{Ga}1}V_{\text{O}2}$	2.26	3.18	1.55	0.54
$V_{\text{Ga}1}V_{\text{O}2} \rightleftharpoons V_{\text{Ga}}^{\text{ia}}V_{\text{O}2}^{\text{a}}$	0.53	0.66	0.63	0.79
$V_{\text{Ga}2}V_{\text{O}2} \rightleftharpoons V_{\text{Ga}}^{\text{ia}}V_{\text{O}2}^{\text{b}}$	0.50	0.36	0.72	0.44

donor means that the negative- $U$  behavior is lost. Thus only the  $V_{\text{Ga}}\text{H}-V_{\text{O}}$  configurations can capture two electrons in the deep Ga–Ga dimer state, resulting in thermodynamic (0/2−) transition levels within the band gap, analogous to the (−/3−) transition levels of  $V_{\text{Ga}}V_{\text{O}}$ . Similarly, the  $V_{\text{Ga}}2\text{H}-V_{\text{O}}$  configurations exhibit a (+/−) transition level, while the  $V_{\text{Ga}}\text{H}-\text{H}_{\text{O}}$  ones do not.

Notably, the thermodynamic (0/2−) and (+/−) transition levels of the hydrogenated divacancies are shifted down in Fermi-level position with respect to the corresponding isolated divacancy levels. This brings the negative- $U$  charge-state transition level into the band gap for some of the config-

urations with Ga2–Ga2 dimers. For example, while  $V_{\text{Ga}}^{\text{ib}}V_{\text{O}1}$  could not be stabilized in the 3− charge state, the thermodynamic (0/2−) level of  $V_{\text{Ga}}^{\text{ib}}\text{H}-V_{\text{O}1}$  occurs 0.22 eV below the CBM. This represents an interesting case where complexing an acceptor with a single shallow donor does not remove an acceptor charge state, but rather introduces an additional acceptor charge state within the band gap. In Ref. [42], we discuss the  $V_{\text{Ga}}^{\text{ib}}\text{H}-V_{\text{O}1}$  complex as a potential defect origin for the so-called  $E_1$  center [5], which has a measured activation energy in the 0.50–0.63 eV range, and appears with a low concentration in the DLTS spectrum of  $\beta\text{-Ga}_2\text{O}_3$  samples annealed in a closed ampoule filled with  $\text{H}_2$  gas at 900 °C.

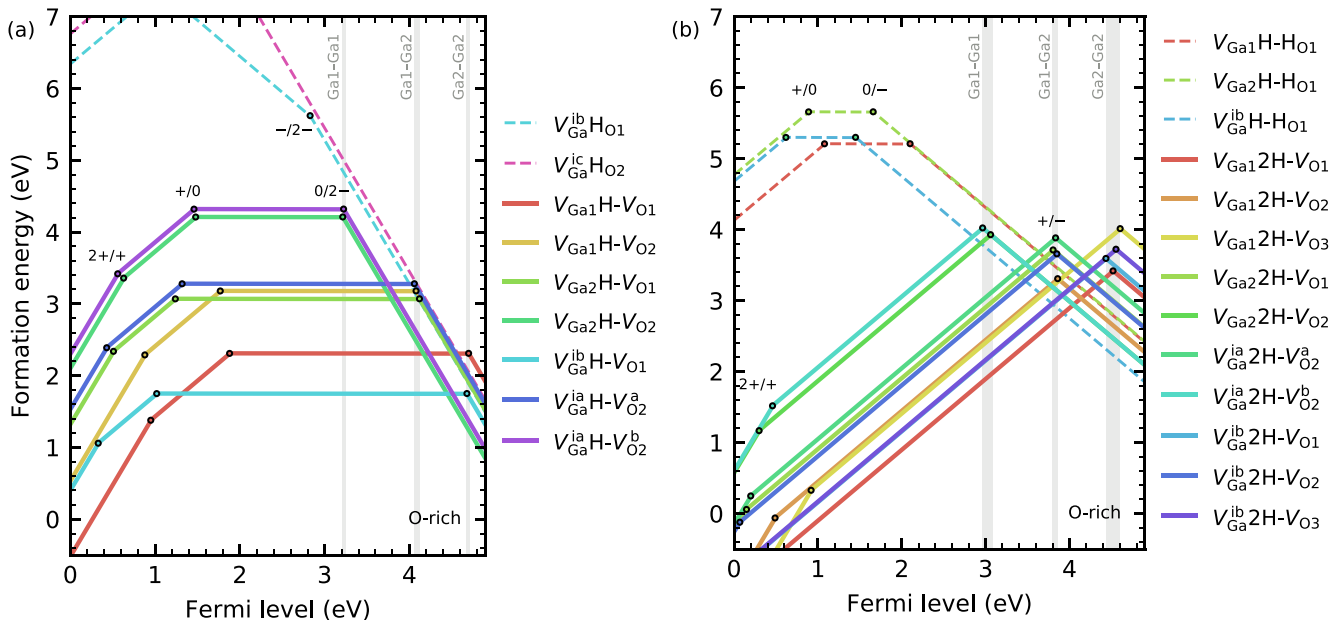


FIG. 3. Formation energies of hydrogenated  $V_{\text{Ga}}V_{\text{O}}$  with (a) one and (b) two H under O-rich conditions for a selection of the most favorable configurations under  $n$ -type and semi-insulating conditions. The grey vertical bars highlight the Fermi level regions with thermodynamic (0/2−) or (+/−) transitions for the three different Ga–Ga dimerizations.

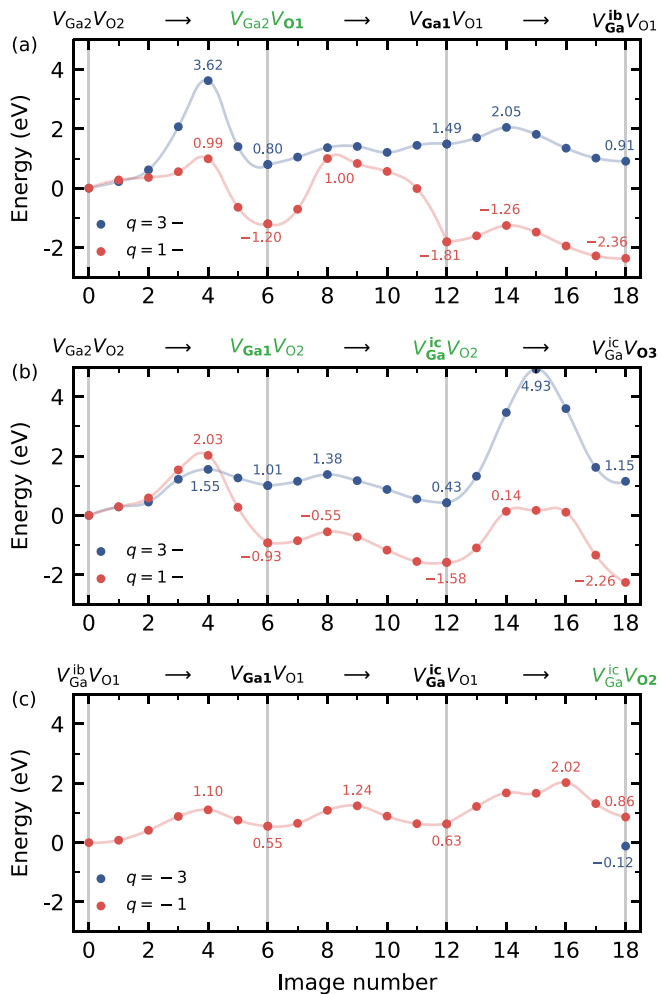


FIG. 4. Calculated energy barriers to transform between different divacancy configurations, starting from the  $V_{\text{Ga}2}V_{\text{O}2}$  configuration with an initial (a) O1 jump and (b) Ga1 jump. [(c) and (b)] The  $V_{\text{Ga}2}V_{\text{O}1}$  configuration can revert back to  $V_{\text{Ga}2}V_{\text{O}2}$  upon zero-bias annealing. Configurations that are compatible with the  $E_2^*$  level are highlighted in green above the plots, and the change after each jump is boldfaced. These calculations included the Ga  $3d$  electrons in the core.

For the doubly hydrogenated divacancies, the corresponding thermodynamic (+/−) levels are shifted even further away from the CBM. On average, the negative- $U$  charge-state transition levels are shifted down by about 0.25 eV per H atom, relative to those of the corresponding isolated divacancy configurations.

For singly hydrogenated divacancies, we find that most configurations prefer to form an O–H bond at  $V_{\text{Ga}}$ . Furthermore, among the  $V_{\text{Ga}}\text{H}_\text{O}$  configurations, only  $V_{\text{Ga}}^{\text{ib}}\text{H}_{\text{O}1}$  and  $V_{\text{Ga}}^{\text{ic}}\text{H}_{\text{O}2}$  are within 1 eV of the lowest energy singly hydrogenated divacancy configurations. As shown in Fig. 4(a), the most energetically favorable configuration is  $V_{\text{Ga}2}\text{H}-V_{\text{O}2}$  or  $V_{\text{Ga}}^{\text{ib}}\text{H}-V_{\text{O}1}$  when the Fermi level is located above or below 4.45 eV, respectively, which is analogous to the  $V_{\text{Ga}2}V_{\text{O}2}$  and  $V_{\text{Ga}}^{\text{ib}}V_{\text{O}1}$  configurations of the isolated divacancy, respectively. For the doubly hydrogenated divacancies, however, we find that the  $V_{\text{Ga}1}2\text{H}-V_{\text{O}1}$  or  $V_{\text{Ga}}^{\text{ib}}\text{H}-\text{H}_{\text{O}1}$  configurations are energetically preferred when the Fermi level is located above or below

3.93 eV, respectively, as shown in Fig. 4(b). Thus the preferred divacancy configuration is changed with respect to the isolated and singly hydrogenated divacancies.

Generally, we find that H prefers bonding to the O ion with the lowest coordination number, which means that, e.g.,  $V_{\text{Ga}}^{\text{ib}}V_{\text{O}1}$  (which has one twofold coordinated O ion) will more strongly bind H than  $V_{\text{Ga}}^{\text{ic}}V_{\text{O}3}$  (which has only threefold coordinated O ions). Moreover, when two O–H bonds are present in the same  $V_{\text{Ga}}$ , there will be Coulomb repulsion between them, decreasing the H binding energy relative to the first H. This repulsion is minimized for divacancies with off-site Ga vacancy configurations (like  $V_{\text{Ga}}^{\text{ib}}V_{\text{O}1}$ ), as the H is shared between two separate Ga vacancies. These considerations help explain why the relative formation energies of different divacancy configurations change as they become hydrogenated, and reflects the complex interplay between local environment and hydrogenation state in determining the relative energetics of a given defect configuration.

Interestingly, the doubly hydrogenated divacancy configuration with the lowest formation energy under  $n$ -type conditions ( $V_{\text{Ga}}^{\text{ib}}\text{H}-\text{H}_{\text{O}1}$ ) is closely related to the  $V_{\text{Ga}}^{\text{ib}}2\text{H}$  complex, which is the lowest energy  $V_{\text{Ga}}2\text{H}$  configuration [5]. The  $V_{\text{Ga}}^{\text{ib}}2\text{H}$  complex has been assigned to an infrared absorption line at  $3437\text{ cm}^{-1}$ , which is the dominant O–H vibrational line observed in  $\beta\text{-Ga}_2\text{O}_3$  samples annealed in  $\text{H}_2$  gas, or exposed to H implantation [40]. Anharmonicity-corrected O–H vibrational frequencies can be calculated from a fourth-order polynomial fit of the potential energy curve calculated for the O–H stretching mode, as explained in Refs. [11,43]. Our calculated vibrational frequency for the O–H bond associated with  $V_{\text{Ga}}^{\text{ib}}\text{H}-\text{H}_{\text{O}1}$  is  $\omega = 3617\text{ cm}^{-1}$  (harmonic component  $\omega_0 = 3849\text{ cm}^{-1}$ , anharmonic shift  $\Delta\omega = 232\text{ cm}^{-1}$ ). This frequency is  $180\text{ cm}^{-1}$  higher than the experimental  $3437\text{ cm}^{-1}$  line assigned to  $V_{\text{Ga}}^{\text{ib}}2\text{H}$  [40]. However, a comparable overestimate of  $181\text{ cm}^{-1}$  was found previously for O–H stretching mode frequencies in  $\text{SnO}_2$  using the same hybrid functional parametrization [43]. If  $181\text{ cm}^{-1}$  is used as a systematic downward shift (as in Refs. [11,43,44]), the calculated frequency for  $V_{\text{Ga}}^{\text{ib}}\text{H}-\text{H}_{\text{O}1}$  is very close to the  $3437\text{ cm}^{-1}$  line, and also exhibits the same orientation and polarization dependence. This suggests that it may be difficult to distinguish  $V_{\text{Ga}}^{\text{ib}}\text{H}-\text{H}_{\text{O}1}$  from  $V_{\text{Ga}}^{\text{ib}}2\text{H}$  using the O–H vibrational stretch modes alone.

To evaluate the thermal stability of the hydrogenated divacancies, H binding energies were calculated by comparing the formation energy of the divacancy before and after trapping a H interstitial, e.g., the H binding energy of  $V_{\text{Ga}2}\text{H}-V_{\text{O}2}$  is given by

$$E_b = [E_f(V_{\text{Ga}2}V_{\text{O}2}) + E_f(\text{H}_i)] - E_f(V_{\text{Ga}2}\text{H}-V_{\text{O}2}). \quad (5)$$

Again, H binding energy diagrams are shown in Ref. [32]. Focusing on the lowest energy configurations in the upper part of the band gap, the calculated H binding energies are 2.48 and 2.34 eV for  $V_{\text{Ga}2}\text{H}-V_{\text{O}2}$  and  $V_{\text{Ga}}^{\text{ib}}\text{H}-\text{H}_{\text{O}1}$  ( $\epsilon_F$  at CBM), and 2.25 and 1.38 eV for  $V_{\text{Ga}}^{\text{ib}}\text{H}-V_{\text{O}1}$  and  $V_{\text{Ga}1}2\text{H}-V_{\text{O}1}$  ( $\epsilon_F$  closer to mid-gap). Thus the singly and doubly hydrogenated divacancies are expected to be thermally stable under relevant Fermi-level positions. In principle, the divacancies could be further complexed with a third hydrogen. However, our calculations for

the  $V_{\text{Ga}}^{\text{ib}}2\text{H-H}_{\text{O}1}$  complex show that it is only stable under  $n$ -type conditions, as the binding energy quickly decreases from 0.85 eV to negative values when the Fermi-level position is lowered from the CBM.

### C. Comparison with DLTS and the $E_2^*$ center

#### 1. Isolated divacancies

In light of the present theoretical predictions, we now discuss the divacancy as a potential defect origin for the  $E_2^*$  center, as suggested previously [8]. Comparing the measured activation energy of about 0.75 eV for the  $E_2^*$  level with the calculated positions of the thermodynamic ( $-/3-$ ) transition levels relative to the CBM, the configurations in the Ga1–Ga2 group are the likeliest candidates. However, care must be taken when comparing calculated thermodynamic charge-state transition levels with activation energies measured by DLTS [45]. First of all, the transitions exhibit negative- $U$  behavior. During conventional DLTS measurements, the activation energy obtained for a negative- $U$  center will correspond to the thermal emission of the first electron [45–47]. For this reason, the activation energy of  $E_2^*$  should be compared with the ( $2-/3-$ ) level of the divacancies. Furthermore, the activation energy deduced from DLTS measurements includes an electron capture barrier, which may be large in some cases. Using a one-dimensional configuration coordinate diagram for the charge-state transition, this barrier can be estimated from the crossing point between the potential energy curves in the initial and final states, as explained in Refs. [35,45]. Adding this barrier to the thermodynamic charge-state transition energy can be considered as an upper estimate for the activation energy measured by DLTS. Indeed, if temperature and quantum mechanical tunneling effects are considered, the effective barrier can be lower, as demonstrated in Ref. [45].

Among the divacancies displayed in Fig. 2(a), there are four configurations in the Ga1–Ga2 group, namely  $V_{\text{Ga}1}V_{\text{O}2}$ ,  $V_{\text{Ga}2}V_{\text{O}1}$ ,  $V_{\text{Ga}}^{\text{ic}}V_{\text{O}2}$ , and  $V_{\text{Ga}}^{\text{ia}}V_{\text{O}2\text{a}}$ . These complexes exhibit thermodynamic ( $2-/3-$ ) levels located 0.79, 0.63, 0.51, and 0.72 eV below the CBM, respectively. If the calculated capture barriers are included, the corresponding activation energies expected to be measured using DLTS are 0.86, 0.86, 0.69, and 0.84 eV. These energies for multiple defect configurations are close to the measured activation energy of about 0.75 eV for  $E_2^*$  determined from DLTS, and also consistent with the possibility of contributions from several overlapping peaks in the DLTS spectrum simulations reported in Ref. [8]. Despite the prospective agreement with  $E_2^*$ , these divacancy configurations are not the most energetically favorable for any Fermi-level position. Based on Fig. 2(a), one would expect  $V_{\text{Ga}2}V_{\text{O}2}/V_{\text{Ga}}^{\text{ia}}V_{\text{O}2\text{a}}$  and  $V_{\text{Ga}}^{\text{ib}}V_{\text{O}1}$  to be the dominant configurations after zero- and reverse-bias annealing, respectively, and none of those configurations are compatible with the  $E_2^*$  level. This raises doubt over the divacancy as a potential defect origin of  $E_2^*$ .

However, as pointed out in Ref. [8], the transformation between different defect configurations may depend on the defect charge state and Fermi-level position and thus play an important role in the formation of the  $E_2^*$  center. To explore this possibility, we use the calculated divacancy transformation barriers in Table I to determine the most likely

configuration to occur after zero- and reverse-bias annealing at 650 K. To simplify the analysis, we assume that the applied reverse-bias voltage effectively causes the Fermi level to shift down from the CBM, such that the divacancy charge states change from  $3-$  to  $1-$ . Based on the results in Ref. [8], the energy barrier to form an  $E_2^*$  compatible configuration must be low enough to be surmounted during reverse-bias annealing ( $T_{\text{a}} \sim 650$  K and  $E_{\text{m}} \sim 1.91$  eV). Moreover, once the  $E_2^*$  compatible configuration has been formed, it should be thermally stable under zero-bias conditions at room temperature ( $T_{\text{a}} \sim 293$  K and  $E_{\text{m}} \sim 0.86$  eV). Finally, a subsequent zero-bias anneal should lead to a partial removal of the  $E_2^*$  compatible configuration, and the formation and removal should be reversible to some extent.

As a starting point, we consider the  $V_{\text{Ga}2}V_{\text{O}2}$  configuration, which is the global-minimum configuration under  $n$ -type conditions (starting from  $V_{\text{Ga}}^{\text{ia}}V_{\text{O}2\text{a}}$ , which is energetically and structurally close to  $V_{\text{Ga}2}V_{\text{O}2}$  would not affect the conclusion from the following analysis). Under zero-bias annealing at 650 K, the Fermi level will be close to the CBM, and the  $3-$  charge state will be preferred for all divacancy configurations exhibiting Ga1–Ga1 or Ga1–Ga2 dimers. If an adjacent Ga1, O1, or O3 atom jumps into the corresponding vacancy, the  $V_{\text{Ga}2}V_{\text{O}2}$  configuration can, in principle, transform into the  $V_{\text{Ga}1}V_{\text{O}2}$ ,  $V_{\text{Ga}2}V_{\text{O}1}$ , or  $V_{\text{Ga}2}V_{\text{O}3}$  configuration, respectively. However, the O jumps exhibit prohibitively large energy barriers in the  $3-$  charge state. Indeed, as seen from the blue line in Fig. 4(a), transformation into  $V_{\text{Ga}2}V_{\text{O}1}$  is associated with a 3.62-eV barrier. Conversely, the Ga1 jump required to reach the  $V_{\text{Ga}1}V_{\text{O}2}$  configuration exhibits a significantly lower migration barrier of 1.55 eV, as seen from the blue line in Fig. 4(b), which should be surmountable at 650 K. Subsequent O jumps again exhibit high migration barriers (3.81 eV to reach  $V_{\text{Ga}1}V_{\text{O}1}$ , not shown), but transformation from  $V_{\text{Ga}1}V_{\text{O}2}$  into the  $V_{\text{Ga}}^{\text{ic}}V_{\text{O}2}$  configuration will be facile (0.37 eV barrier). At this point, the transformation stops, because the subsequent O jumps exhibit prohibitively high migration barriers [4.50 eV to reach  $V_{\text{Ga}}^{\text{ic}}V_{\text{O}3}$ , as shown in Fig. 4(b)]. The  $V_{\text{Ga}1}V_{\text{O}2}$  and  $V_{\text{Ga}}^{\text{ic}}V_{\text{O}2}$  configurations are compatible with the  $E_2^*$  level, but their equilibrium concentrations should be low owing to energies in  $n$ -type conditions that are 1.01 and 0.43 eV higher than the  $V_{\text{Ga}2}V_{\text{O}2}$ , respectively, as seen in Fig. 4(b). Additionally, owing to the small barriers seen in Fig. 4(b), these metastable species would preferentially convert to  $V_{\text{Ga}2}V_{\text{O}2}$ , which are expected to remain the dominant configuration in  $n$ -type conditions.

Next, we consider reverse-bias annealing at 650 K from the same  $V_{\text{Ga}2}V_{\text{O}2}$  starting point, under the assumption that all divacancy configurations occur in the  $1-$  charge state, summarized as the red paths in Figs. 4(a) and 4(b). The situation is now reversed for the initial O and Ga jumps, respectively. The transformation from  $V_{\text{Ga}2}V_{\text{O}2}$  to the  $V_{\text{Ga}1}V_{\text{O}2}$  configuration is now associated with a higher energy barrier of 2.03 eV, but the barrier to reach the  $V_{\text{Ga}2}V_{\text{O}1}$  configuration is significantly lowered to 0.99 eV. Interestingly, after the latter jump, the energy barrier to proceed from  $V_{\text{Ga}2}V_{\text{O}1}$  to another divacancy configuration is at least 2.20 eV. If the temperature is sufficiently high for this barrier to be surmounted, the global-minimum  $V_{\text{Ga}}^{\text{ib}}V_{\text{O}1}$  configuration can be reached easily via  $V_{\text{Ga}1}V_{\text{O}1}$ . However, it is unlikely that the 2.20 eV barrier

will be surmounted at 650 K, which means that the local minimum and  $E_2^*$  compatible  $V_{\text{Ga}_2}\text{V}_{\text{O}_1}$  configuration will be frozen in. The  $V_{\text{Ga}_2}\text{V}_{\text{O}_1}$  configuration should also be thermally stable under zero-bias experimental conditions, as accessing lower-energy configurations like the  $V_{\text{Ga}}^{\text{ib}}\text{V}_{\text{O}_1}$  in  $n$ -type material should be unlikely at room temperature, owing to thermal barriers of at least 1.25 eV [Fig. 4(b)]. Thus reverse-bias annealing at 650 K from  $V_{\text{Ga}_2}\text{V}_{\text{O}_2}$  is expected to lead to the formation of an  $E_2^*$  compatible configuration ( $V_{\text{Ga}_2}\text{V}_{\text{O}_1}$ ), in line with the experiments [8].

Finally, we consider a subsequent zero-bias anneal at 650 K with the  $V_{\text{Ga}_2}\text{V}_{\text{O}_1}$  configuration as a starting point. Now, the global-minimum configuration is  $V_{\text{Ga}_2}\text{V}_{\text{O}_2}$ . This configuration cannot be reached with a single O2 jump from the initial  $V_{\text{Ga}_2}\text{V}_{\text{O}_1}$  state, as the transformation energy barrier is 2.82 eV [Fig. 4(a)]. However, as shown in Fig. 4(c), the global-minimum  $V_{\text{Ga}_2}\text{V}_{\text{O}_2}$  configuration can be reached through a series of jumps with an overall barrier of 2.02 eV (note that the  $V_{\text{Ga}}^{\text{ib}}\text{V}_{\text{O}_1}$ ,  $V_{\text{Ga}}\text{V}_{\text{O}_1}$ , and  $V_{\text{Ga}}^{\text{ic}}\text{V}_{\text{O}_1}$  configurations in Fig. 4(c) prefer the  $1-$  charge-state even under  $n$ -type conditions). This would account for the observed reversible formation and removal of  $E_2^*$ . However, if the zero-bias annealing temperature is not high enough to convert  $V_{\text{Ga}_2}\text{V}_{\text{O}_1}$  back into the lowest energy  $V_{\text{Ga}_2}\text{V}_{\text{O}_2}$  configuration, there will instead be an equilibrium between the  $V_{\text{Ga}_2}\text{V}_{\text{O}_1}$  and  $V_{\text{Ga}_1}^{\text{ib}}\text{V}_{\text{O}_1}$  configurations [Fig. 4(a)], which differ in energy by merely 0.11 eV in the  $3-$  charge state. Then, only partial removal of the  $E_2^*$  compatible  $V_{\text{Ga}_2}\text{V}_{\text{O}_1}$  configuration will result from the zero-bias annealing, and subsequent reverse-bias annealing will not reform  $E_2^*$ . The analysis above shows that an asymmetry in the divacancy transformation kinetics for zero- versus reverse-bias annealing could be possible. However, further experiments will be necessary to verify the model. For example, reverse-bias annealing at even higher temperatures would allow the abovementioned  $V_{\text{Ga}_2}\text{V}_{\text{O}_1}$  to reach the lowest energy  $V_{\text{Ga}_1}^{\text{ib}}\text{V}_{\text{O}_1}$  configuration, which means that reverse-bias annealing should promote  $E_2^*$  only up to a certain temperature ( $\sim 750$  K, based on the 2.20 eV barrier to escape from  $V_{\text{Ga}_2}\text{V}_{\text{O}_1}$ ). Furthermore, the divacancy model implies negative- $U$  behavior, which might be possible to explore experimentally, e.g., using the approach outlined in Ref. [46].

## 2. Hydrogenated divacancies

Our recent experiments suggest that the  $E_2^*$  center will interact with H [8]. Specifically, H implantation does not seem to influence the introduction of  $E_2^*$  during the subsequent reverse-bias anneal, but the removal of  $E_2^*$  during the zero-bias anneal is strongly promoted [8], i.e., a significantly higher degree of reversibility is observed for H compared to He implantation. An explanation for this could be that  $E_2^*$  is passivated by H under zero-bias conditions, and that this complex becomes unstable under reverse-bias conditions, resulting in reorientation of the hydrogenated center, and reappearance of  $E_2^*$ . Importantly, the pronounced difference between He and H implantations suggests that most  $E_2^*$  centers interact with H. For this reason, under the assumption of a divacancy model for  $E_2^*$ , predominantly the hydrogenated divacancies are expected to play a role for H implantation, while the isolated divacancies are unlikely to occur. This is consis-

tent with the calculated H binding energies for hydrogenated divacancies, which are comparable in magnitude to those calculated previously for  $V_{\text{Ga}}$  [15], which is a dominant H trap in  $\beta$ - $\text{Ga}_2\text{O}_3$  [40].

Some of the doubly hydrogenated divacancies with Ga2–Ga2 dimerization exhibit thermodynamic charge-state transition levels that are close to the measured activation energy of about 0.75 eV for the  $E_2^*$  center, including the  $V_{\text{Ga}_1}2\text{H}-\text{V}_{\text{O}_1}$  and  $V_{\text{Ga}}^{\text{ib}}2\text{H}-\text{V}_{\text{O}_1}$  configurations. Considering the thermodynamic ( $0/-$ ) transitions, these complexes exhibit levels located 0.66 and 0.70 eV below the CBM, respectively. When the capture barrier is included for comparison with the DLTS results, the energies rise to 0.75 eV for the  $V_{\text{Ga}_1}2\text{H}-\text{V}_{\text{O}_1}$  and 0.78 eV for the  $V_{\text{Ga}}^{\text{ib}}2\text{H}-\text{V}_{\text{O}_1}$ , making both hydrogenated configurations excellent candidates for the  $E_2^*$  center.

We now envision the reorientation of doubly hydrogenated divacancies expected during zero- and reverse-bias annealing at 650 K. Under zero-bias annealing conditions, the Fermi level will be close to the CBM, and the  $V_{\text{Ga}}^{\text{ib}}\text{H}-\text{H}_{\text{O}_1}$  configuration will be energetically preferred. This configuration does not exhibit any thermodynamic charge-state transition levels near the CBM, consistent with the removal of  $E_2^*$  after zero-bias annealing in H-implanted samples [8]. During reverse-bias annealing, however, the  $E_2^*$  compatible  $V_{\text{Ga}_1}2\text{H}-\text{V}_{\text{O}_1}$  configuration is predicted to be lowest in energy. Note that this is in contrast to the isolated divacancies, where the  $E_2^*$  compatible configurations are not lowest in formation energy for any Fermi level position. A possible scenario is that  $V_{\text{Ga}}^{\text{ib}}\text{H}-\text{H}_{\text{O}_1}$  transforms into the  $E_2^*$  compatible  $V_{\text{Ga}}^{\text{ib}}2\text{H}-\text{V}_{\text{O}_1}$  configuration upon reverse-bias annealing, which only requires a single H jump. However, the  $V_{\text{Ga}}^{\text{ib}}2\text{H}-\text{V}_{\text{O}_1}$  configuration must then be thermally stable at room temperature. Our CI-NBE calculations show that the migration barrier to go back from  $V_{\text{Ga}}^{\text{ib}}2\text{H}-\text{V}_{\text{O}_1}$  to  $V_{\text{Ga}}^{\text{ib}}\text{H}-\text{H}_{\text{O}_1}$  in the  $1-$  charge state is 0.99 eV. This scenario could thus explain the higher degree of reversibility observed for the formation and removal of  $E_2^*$  in the presence of H.

To summarize, the divacancy remains a promising candidate for the defect origin of the  $E_2^*$  center. Specifically, the present hybrid functional calculations point to the isolated  $V_{\text{Ga}_1}\text{V}_{\text{O}_2}$ ,  $V_{\text{Ga}_2}\text{V}_{\text{O}_1}$ ,  $V_{\text{Ga}}^{\text{ic}}\text{V}_{\text{O}_2}$ , and  $V_{\text{Ga}}^{\text{ia}}\text{V}_{\text{O}_2\text{a}}$  divacancy configurations, and the doubly hydrogenated  $V_{\text{Ga}}^{\text{ib}}2\text{H}-\text{V}_{\text{O}_1}$  and  $V_{\text{Ga}_1}2\text{H}-\text{V}_{\text{O}_1}$  divacancy configurations as the most likely candidates. Importantly, we find that the divacancy can explain the reversible formation and removal of  $E_2^*$  during reverse- and zero-bias annealing, respectively, as well as the significantly higher degree of reversibility observed in the presence of H [8]. However, further experiments are required to verify the model.

## IV. CONCLUSION

Using hybrid functional calculations, we have explored the relative stability and electrical properties of 19 different  $V_{\text{Ga}}\text{V}_{\text{O}}$  configurations. The calculated formation energy of the divacancy is relatively low under  $n$ -type (and especially O-rich) conditions. This means the divacancy could be found in appreciable concentrations in  $\beta$ - $\text{Ga}_2\text{O}_3$ , depending on the crystal growth method and sample history, which should be considered when interpreting experimental data. The divacancy is



found to be highly electrically active, exhibiting charge states ranging from  $2+$  to  $1-$  or  $3-$ . The transition from  $1-$  to  $3-$  exhibits negative- $U$ , similar to the isolated  $V_O$ , and the  $3-$  charge state is associated with the formation of a deep Ga–Ga dimer state. The negative- $U$  transition levels occur within two narrow Fermi level ranges, where the common feature of the configurations in each range is the type of Ga–Ga dimer (Ga1 or Ga2 sites). Hydrogenation of the divacancy is found to either passivate the negative- $U$  charge-state transition levels, or shift them down in Fermi level position, depending on whether H resides at  $V_O$  or forms an O–H bond at  $V_{Ga}$ . The latter H configuration is found to be energetically preferred for the singly hydrogenated divacancies. For the doubly hydrogenated divacancies, however, the  $H_O$  configuration becomes more favorable for certain divacancy configurations under  $n$ -type conditions, including the global-minimum  $V_{Ga}^{ib}H-H_{O1}$  configuration.

The calculations support  $V_{Ga}V_O$  as a potential origin of the  $E_2^*$  center, as suggested previously [8]. Specifically, the  $V_{Ga1}VO_2$ ,  $V_{Ga2}VO_1$ ,  $V_{Ga}^{ic}VO_2$  and  $V_{Ga}^{ia}VO_{2a}$ ,  $V_{Ga}^{ib}2HV_{O1}$  and  $V_{Ga1}2HV_{O1}$  complexes were found to be the most promising candidates. The Fermi level and temperature dependence of the transformation between different divacancy configurations and H positions is found to play a key role. However, further experimental work will be required to verify the divacancy model. More generally, it seems that Ga–Ga dimer states can exhibit charge-state transition levels close to the CBM. Indeed, a similar Ga–Ga dimer state is formed by the singly

positively charged Ga interstitial, which exhibits a corresponding thermodynamic ( $3+/+$ ) transition level close to the CBM [48]. This family of defects states could be responsible for other intrinsic electron traps observed by DLTS [5]. This work also serves to highlight the importance of sample history in understanding and controlling defect populations in  $Ga_2O_3$ -based devices.

## ACKNOWLEDGMENTS

Financial support was kindly provided by the Research Council of Norway and University of Oslo through the frontier research project FUNDAMeNT (Grant No. 251131, FriPro ToppForsk-program), the Research Center for Sustainable Solar Cell Technology (Grant No. 257639, FME SUSOLTECH), and the Faculty of Mathematics and Natural Sciences at the University of Oslo via the strategic research initiative FOXHOUND. The computations were performed on resources provided by UNINETT Sigma2 - the National Infrastructure for High Performance Computing and Data Storage in Norway. This work was partially performed under the auspices of the US DOE by Lawrence Livermore National Laboratory under Contract No. DE-AC52-07NA27344, and supported by the Critical Materials Institute, an Energy Innovation Hub funded by the US DOE, Office of Energy Efficiency and Renewable Energy, Advanced Manufacturing Office.

- [1] M. Higashiwaki and G. H. Jessen, *Appl. Phys. Lett.* **112**, 060401 (2018).
- [2] M. D. McCluskey, *J. Appl. Phys.* **127**, 101101 (2020).
- [3] J. F. McGlone, Z. Xia, C. Joishi, S. Lodha, S. Rajan, S. Ringel, and A. R. Arehart, *Appl. Phys. Lett.* **115**, 153501 (2019).
- [4] J. F. McGlone, Z. Xia, Y. Zhang, C. Joishi, S. Lodha, S. Rajan, S. A. Ringel, and A. R. Arehart, *IEEE Electron Device Lett.* **39**, 1042 (2018).
- [5] M. E. Ingebrigtsen, A. Y. Kuznetsov, B. G. Svensson, G. Alfieri, A. Mihaila, U. Badstübner, A. Perron, L. Vines, and J. B. Varley, *APL Mater.* **7**, 022510 (2019).
- [6] M. E. Ingebrigtsen, J. B. Varley, A. Y. Kuznetsov, B. G. Svensson, G. Alfieri, A. Mihaila, U. Badstübner, and L. Vines, *Appl. Phys. Lett.* **112**, 042104 (2018).
- [7] C. Zimmermann, Y. K. Frodason, A. W. Barnard, J. B. Varley, K. Irmscher, Z. Galazka, A. Karjalainen, W. E. Meyer, F. D. Auret, and L. Vines, *Appl. Phys. Lett.* **116**, 072101 (2020).
- [8] C. Zimmermann, E. F. Verhoeven, Y. K. Frodason, P. M. Weiser, J. B. Varley, and L. Vines, *J. Phys. D* **53**, 464001 (2020).
- [9] N. T. Son, Q. D. Ho, K. Goto, H. Abe, T. Ohshima, B. Monemar, Y. Kumagai, T. Frauenheim, and P. Deák, *Appl. Phys. Lett.* **117**, 032101 (2020).
- [10] J. B. Varley, J. R. Weber, A. Janotti, and C. G. Van de Walle, *Appl. Phys. Lett.* **97**, 142106 (2010).
- [11] J. B. Varley, H. Peelaers, A. Janotti, and C. G. V. de Walle, *J. Phys. Condens. Matter* **23**, 334212 (2011).
- [12] T. Zacherle, P. C. Schmidt, and M. Martin, *Phys. Rev. B* **87**, 235206 (2013).
- [13] A. Kyrtos, M. Matsubara, and E. Bellotti, *Phys. Rev. B* **95**, 245202 (2017).
- [14] P. Deák, Q. Duy Ho, F. Seemann, B. Aradi, M. Lorke, and T. Frauenheim, *Phys. Rev. B* **95**, 075208 (2017).
- [15] J. B. Varley, First-principles calculations 2, in *Gallium Oxide: Materials Properties, Crystal Growth, and Devices*, edited by M. Higashiwaki and S. Fujita (Springer International Publishing, Cham, 2020), pp. 329–348.
- [16] M. S. Holston, E. M. Golden, B. E. Kananen, J. W. McClory, N. C. Giles, and L. E. Halliburton, *J. Appl. Phys.* **119**, 145701 (2016).
- [17] I. L. Kolevatov, B. G. Svensson, and E. V. Monakhov, *J. Appl. Phys.* **124**, 085706 (2018).
- [18] P. E. Blöchl, *Phys. Rev. B* **50**, 17953 (1994).
- [19] G. Kresse and D. Joubert, *Phys. Rev. B* **59**, 1758 (1999).
- [20] G. Kresse and J. Furthmüller, *Phys. Rev. B* **54**, 11169 (1996).
- [21] A. V. Krukau, O. A. Vydrov, A. F. Izmaylov, and G. E. Scuseria, *J. Chem. Phys.* **125**, 224106 (2006).
- [22] Y. K. Frodason, K. M. Johansen, L. Vines, and J. B. Varley, *J. Appl. Phys.* **127**, 075701 (2020).
- [23] C. Janowitz, V. Scherer, M. Mohamed, A. Krapf, H. Dwelk, R. Manzke, Z. Galazka, R. Uecker, K. Irmscher, R. Fornari, M. Michling, D. Schmeißer, J. R. Weber, J. B. Varley, and C. G. V. de Walle, *New J. Phys.* **13**, 085014 (2011).
- [24] S. Geller, *J. Chem. Phys.* **33**, 676 (1960).
- [25] C. Freysoldt, B. Grabowski, T. Hickel, J. Neugebauer, G. Kresse, A. Janotti, and C. G. Van de Walle, *Rev. Mod. Phys.* **86**, 253 (2014).
- [26] J. B. Varley, A. Janotti, C. Franchini, and C. G. Van de Walle, *Phys. Rev. B* **85**, 081109(R) (2012).
- [27] Y. Kumagai and F. Oba, *Phys. Rev. B* **89**, 195205 (2014).

- [28] C. Freysoldt, J. Neugebauer, and C. G. Van de Walle, *Phys. Rev. Lett.* **102**, 016402 (2009).
- [29] M. Schubert, R. Korlacki, S. Knight, T. Hofmann, S. Schöche, V. Darakchieva, E. Janzén, B. Monemar, D. Gogova, Q.-T. Thieu, R. Togashi, H. Murakami, Y. Kumagai, K. Goto, A. Kuramata, S. Yamakoshi, and M. Higashiwaki, *Phys. Rev. B* **93**, 125209 (2016).
- [30] G. Henkelman, B. P. Uberuaga, and H. Jansson, *J. Chem. Phys.* **113**, 9901 (2000).
- [31] S. Pearton, J. Yang, P. Cary, F. Ren, J. Kim, M. Tadjer, and M. Mastro, *Appl. Phys. Rev.* **5**, 011301 (2018).
- [32] See Supplemental Material at <http://link.aps.org/supplemental/10.1103/PhysRevMaterials.5.025402> for removal and formation energy diagrams of all explored isolated and hydrogenated divacancy configurations, and the saddle point structures from the CI-NEB calculations.
- [33] P. W. Anderson, *Phys. Rev. Lett.* **34**, 953 (1975).
- [34] A. M. Stoneham and M. J. L. Sangster, *Radiat. Eff.* **73**, 267 (1983).
- [35] Y. K. Frodason, K. M. Johansen, A. Alkauskas, and L. Vines, *Phys. Rev. B* **99**, 174106 (2019).
- [36] A. Janotti and C. G. Van de Walle, *Phys. Rev. B* **76**, 165202 (2007).
- [37] F. Oba, A. Togo, I. Tanaka, J. Paier, and G. Kresse, *Phys. Rev. B* **77**, 245202 (2008).
- [38] J. L. Lyons, J. B. Varley, D. Steiauf, A. Janotti, and C. G. V. de Walle, *J. Appl. Phys.* **122**, 035704 (2017).
- [39] D. Steiauf, J. L. Lyons, A. Janotti, and C. G. Van de Walle, *APL Mater.* **2**, 096101 (2014).
- [40] P. Weiser, M. Stavola, W. B. Fowler, Y. Qin, and S. Pearton, *Appl. Phys. Lett.* **112**, 232104 (2018).
- [41] Y. Qin, M. Stavola, W. B. Fowler, P. Weiser, and S. J. Pearton, *ECS J. Solid State Sci. Technol.* **8**, Q3103 (2019).
- [42] C. Zimmermann, E. F. Verhoeven, P. M. Weiser, Y. K. Frodason, J. B. Varley, I. Kolevatski, and L. Vines (unpublished).
- [43] W. M. Hlaing Oo, S. Tabatabaei, M. D. McCluskey, J. B. Varley, A. Janotti, and C. G. Van de Walle, *Phys. Rev. B* **82**, 193201 (2010).
- [44] J. R. Ritter, J. Huso, P. T. Dickens, J. B. Varley, K. G. Lynn, and M. D. McCluskey, *Appl. Phys. Lett.* **113**, 052101 (2018).
- [45] D. Wickramaratne, C. E. Dreyer, B. Monserrat, J.-X. Shen, J. L. Lyons, A. Alkauskas, and C. G. Van de Walle, *Appl. Phys. Lett.* **113**, 192106 (2018).
- [46] C. G. Hemmingsson, N. T. Son, A. Ellison, J. Zhang, and E. Janzén, *Phys. Rev. B* **58**, R10119 (1998).
- [47] N. T. Son, X. T. Trinh, L. S. Løvlie, B. G. Svensson, K. Kawahara, J. Suda, T. Kimoto, T. Umeda, J. Isoya, T. Makino, T. Ohshima, and E. Janzén, *Phys. Rev. Lett.* **109**, 187603 (2012).
- [48] C. Zimmermann, V. Rønning, Y. Kalmann Frodason, V. Bobal, L. Vines, and J. B. Varley, *Phys. Rev. Mater.* **4**, 074605 (2020).